Chapter 3 ***Structure, Optical and Magnetic Properties with electrochemical Performance of α and β-MnO_2Nanorods***

3.1 Introduction

In this chapter, different phases such as α, β, and mixed phase of α and β-MnO_2 by varying the concentration of potassium ion are synthesized by hydrothermal technique. Further, we discuss the detailed investigations on their structural, microstructural, optical, magnetic and electrochemical properties. In section 3.2.1 and 3.2.2, FT-IR spectra and XRD patterns of α, β, and mixed phase of α and β-MnO_2 have been analyzed to verify the phase. SEM micrographs reveals that the polymorphic phases are crystalizes in the form of nanorods, as illustrated in section 3.2.3. Section 3.2.4 and 3.2.5 investigate the optical band gap and oxygen vacancies of samples obtained from UV visible spectroscopy and X-ray photoelectron spectroscopy, respectively. Electrochemical performances through cyclic voltammetry are explained in section 3.3. Detailed investigations on magnetic properties understanding their magnetic transitions and spin-glass behaviour based on different concentration of Mn^{3+}/Mn^{4+} in each sample has been discussed in section 3.3. In section 3.4, we conclude that SG/cluster-glass behaviour is critical towards the presence of Mn^{3+} in MnO_2 compound.

3.2 Structure, Microstructure and Optical Properties

3.2.1 Fourier Transform Infrared Spectroscopy

Fourier transform infrared spectroscopy (FT-IR) depicted in figure 3.1 show the absorption bands at 3430, 1635, 1371, 1254, 1201, 1163 and 828 cm^{-1}, in α, β and αβ-MnO_2. Stretching vibrations of the surface hydroxyl group of nanoparticles (Mn-OH) and bending vibrations of H-O-H groups from the absorbed water molecules are represented by the broad peak around 3430 cm^{-1}, and 1635 cm^{-1}, respectively. The weak absorption band

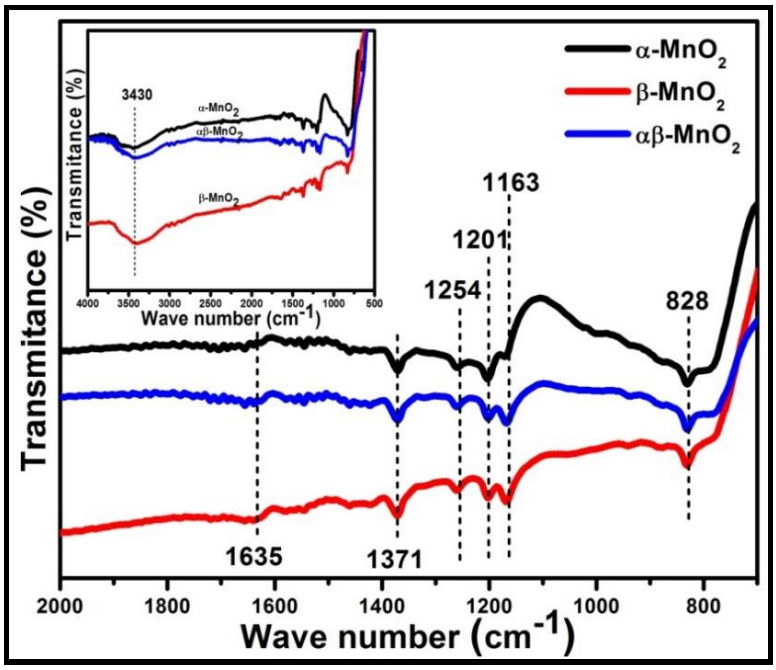

Figure 3.1: *Fourier-Transform Infrared (FT-IR) spectrum of α-MnO_2, β- MnO_2 and αβ-MnO_2 nanorods.*

observed around 1254, 1201 and 1163 are attributed to the bending vibrations of the hydroxyl group (–OH) combined with Mn atoms. 1371 cm^{-1} is ascribed to O-Mn-O vibrations of MnO_2. Moreover, the high intense band corresponding to 828 cm^{-1} indicates Mn-O vibrations in MnO_6 octahedral units in different phases of MnO_2. FT-IR results confirm that all the samples are of MnO_2 rich in surface hydroxyl group.

3.2.2 X-Ray Diffraction: Rietveld Refinement

To determine the crystal structure of the synthesized products, we perform X-ray diffraction at room temperature. Depending on the synthesis parameters and precursors used, XRD patterns of all samples prepared via hydrothermal route are displayed in figure 3.2. Prominent Bragg diffraction peaks corresponds to (110), (200), (220), (310), (211), (420), (321), (411), (060), (251), and (451) are indexed to the tetragonal phase of α-MnO_2 (JCPDS No. 44-0141) with space group I4/m (figure 3.2(a)). On changing the concentration of $KMnO_4$ from 1M to 0.1M, figure 3.2(b) depicts the diffraction peaks along with a sharp peak at 26.23° ascribed to $(11\bar{1})$ of monoclinic phase of γ-MnOOH (JCPDS NO. 41-1379). Under prolonged reaction carried out in a magnetic stirrer for 12 h, two different crystalline phases of MnO_2 are observed. Two phases are α-MnO_2 (I4/m, JCPDS No. 44-0141) and β-MnO_2 (p42/mnm, JCPDS No. 240735) as shown in figure 3.2(c), named as αβ-MnO_2 throughout the text. Calcining then sample at 400°C for 4 hours, no structural changes are observed for α-MnO_2 and αβ-MnO_2 nanorods (figure 3.3) except γ-MnOOH. Thermal oxidation of γ-MnOOH leads to the formation of β-MnO_2, $p4_2/mnm$. Similar results have been reported by *Wei et. al.* where transformation of γ-MnOOH to the β phase of MnO_2 on annealing at 400°C is obtained [97]. Moreover, no other Bragg diffraction peaks corresponding to the impurity phase have been observed in all samples

manifesting that pure phases of α-MnO_2, β-MnO_2 and αβ-MnO_2 are synthesized successfully.

Further, we have used Rietveld refinement of Fullprof program considering pseudo-Voigt function to fit the XRD patterns. The results are shown in figure 3.4. The experimental pattern, calculated data and their difference are represented by solid line, dotted and continuous line, respectively. The position of Bragg reflection peaks represented by tick marks above the difference pattern indicates. The small value of χ^2 (goodness of fit) and the difference plot (shown by blue line) signifies that the Rietveld refinement of all samples is fairly satisfactory. The refined lattice parameters and atomic fractional coordinates obtained from the refinement are given in Table 3.1.

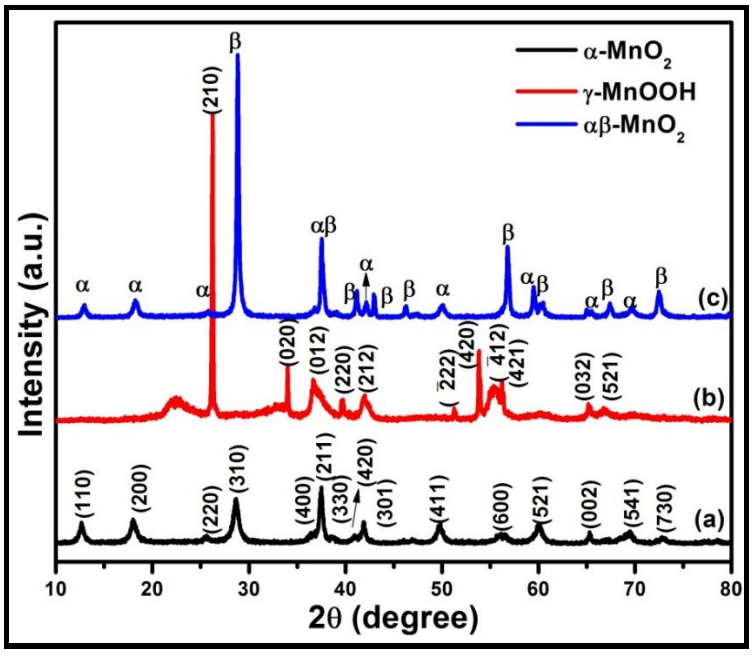

Figure 3.2: *Room temperature X-Ray diffraction (XRD) pattern of (a) α-MnO_2, (b) γ-MnOOH, and (c) αβ- MnO_2 nanorods.*

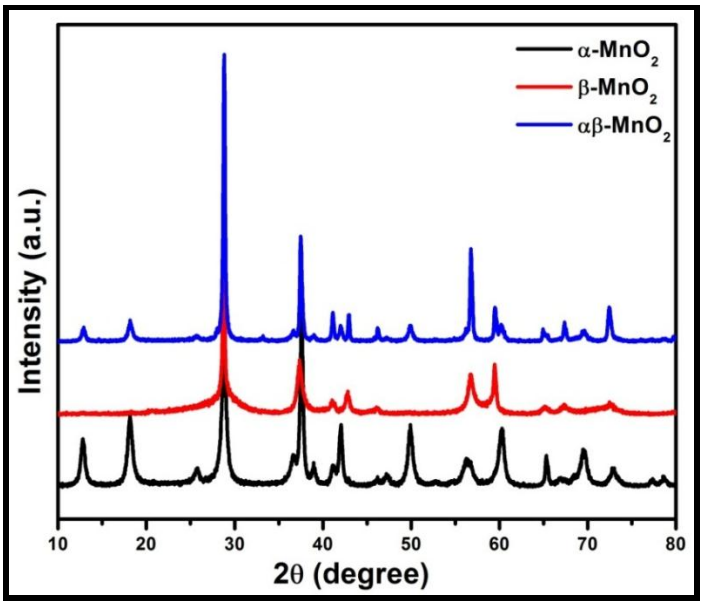

Figure 3.3: *X-Ray diffraction (XRD) pattern of α-MnO_2, β-MnO_2, and αβ- MnO_2 nanorods calcined at 400° C.*

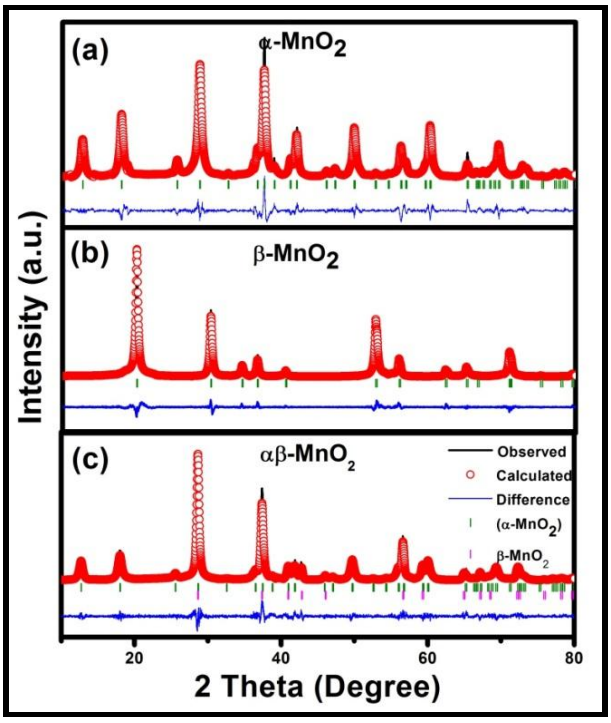

Figure 3.4: *XRD pattern of α-MnO_2, β- MnO_2 and αβ- MnO_2 nanorods fitted using Rietveld refinement of Fullprof program.*

Table 3.1: Structural parameters obtained from Rietveld refinement fitting for (a) α-MnO_2, (b) β-MnO_2 and (c) αβ- MnO_2 nanorods.

(a) α-MnO_2

S.G. *I4/m*, a=b= 9.8187 (15) Å and c= 2.8591 (4) Å, α=β=γ=90°, V= 275.63 (7)				
Atom	**x**	**y**	**z**	**Occupancy**
Mn	0.3554 (5)	0.1718 (6)	0.00	1
O1	0.1593 (17)	0.178 (2)	0.00	1
O2	0.538(2)	0.1612 (18)	0.00	0.7761
K	0.00	0.00	0.50	0.8084
R_p= 16 %, R_{wp}= 20 % and χ^2= 2.71				

(b) β-MnO_2

S.G. *$P4_2/mnm$*, a=b= 4.399 (2) Å and c= 2.875 (18) Å, α=β=γ=90°, V= 55.665 (5)				
Atom	**x**	**y**	**z**	**Occupancy**
Mn	0	0	0.00	1
O	0.3010 (8)	0.3010 (8)	0.00	2
R_p= 15.9 %, R_{wp}= 18.9 % and χ^2= 1.95				

(c) αβ-MnO_2

Phase 1-S.G. *I4/m*, a=b= 9.8454 (14) Å and c= 2.8619 (6) Å, α=β=γ=90°, V= 277.41 (8) Phase 2-S.G. *$P4_2/mnm$*, a=b= 4.4063 (5) Å and c= 2.8717 (4) Å, α=β=γ=90°, V= 55.755 (12)					
	Atom	**x**	**y**	**z**	**Occupancy (N)**
Phase 1 α-MnO_2	**Mn**	0.3446 (10)	0.1622 (11)	0.00	1
	O1	0.1471 (18)	0.2019 (19)	0.00	1
	O2	0.541 (2)	0.1670 (18)	0.00	1
	K	0.00	0.00	0.50	0.916 (17)
Phase 2 β-MnO_2	**Mn**	0.00	0.00	0.00	1
	O	0.2917 (20)	0.2917 (20)	0.00	2
R_p= 21.4 %, R_{wp}= 27.4 % and χ^2= 1.37					

It is observed that while lattice expansion occurs in α-MnO_2, in β-MnO_2, no change in lattice volume could be detected [102]. Further, we estimate the phase fraction in mixed phase which is found to be 73.35% of α and 26.65% of β phase of MnO_2. It is to be noted that we could synthesize mixed phase by varying the concentration of $KMnO_4$ and stirring the solution throughout the hydrothermal dwell time without using any phase transforming agent as used by *Zhang et al.* [99].

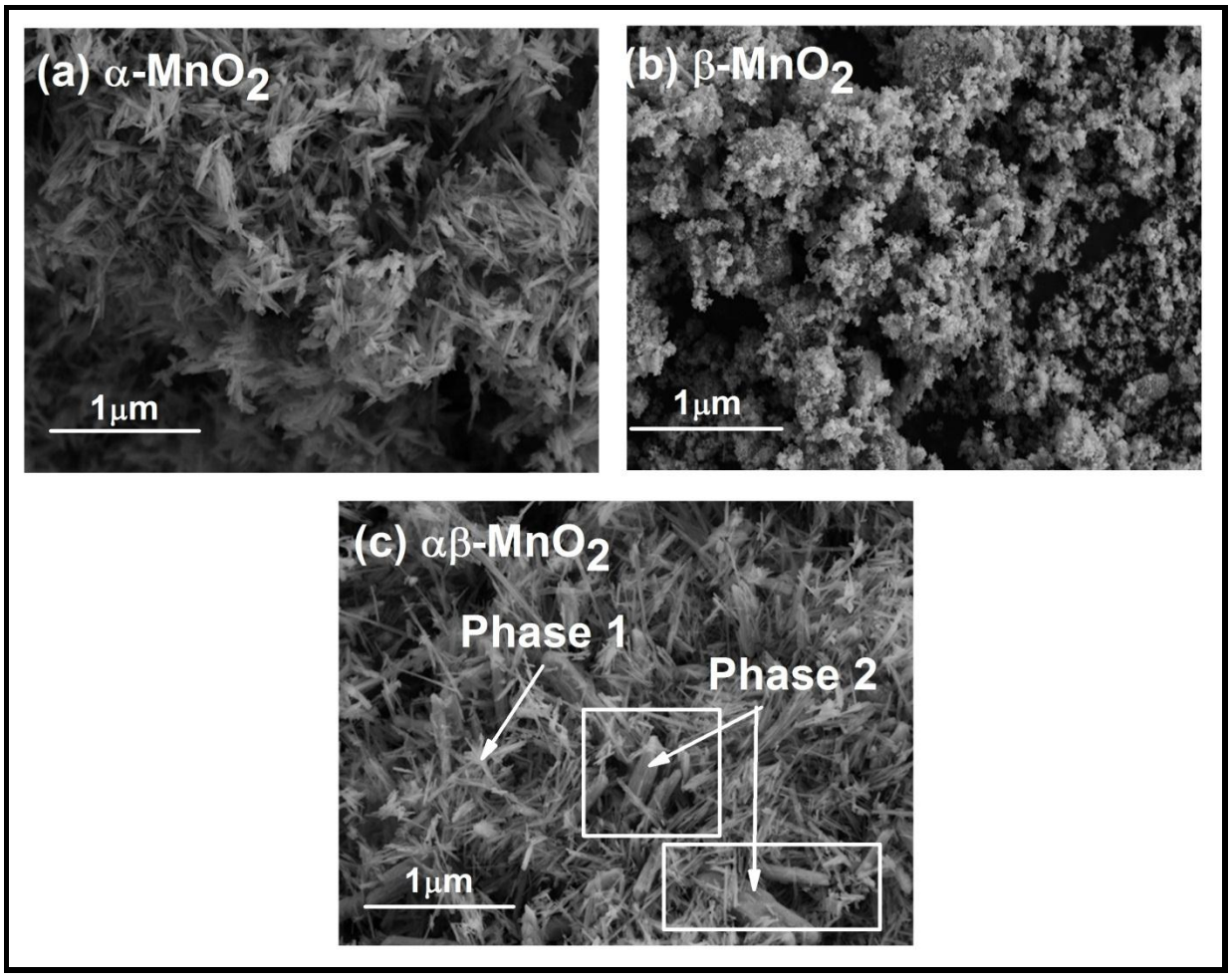

Figure 3.5: *Scanning electron micrograph (SEM) of (a) α-MnO_2, (b) β- MnO_2 and (c) αβ-MnO_2 nanorods.*

3.2.3 Emission Scanning Electron Microscope

Field emission scanning electron micrographs demonstrate nanorods of variable dimensions irrespective of phases shown in figure 3.5. Average diameter of α-MnO_2 and β-MnO_2 nanorods calculated through particle size distribution histogram is found to be 36 and 23 nm, respectively (figure 3.6). Further, we extract nanorods of two different sizes, 28 and 116 nm present in figure 3.6(c1 & c2) which may attribute to the two different phases of MnO_2.

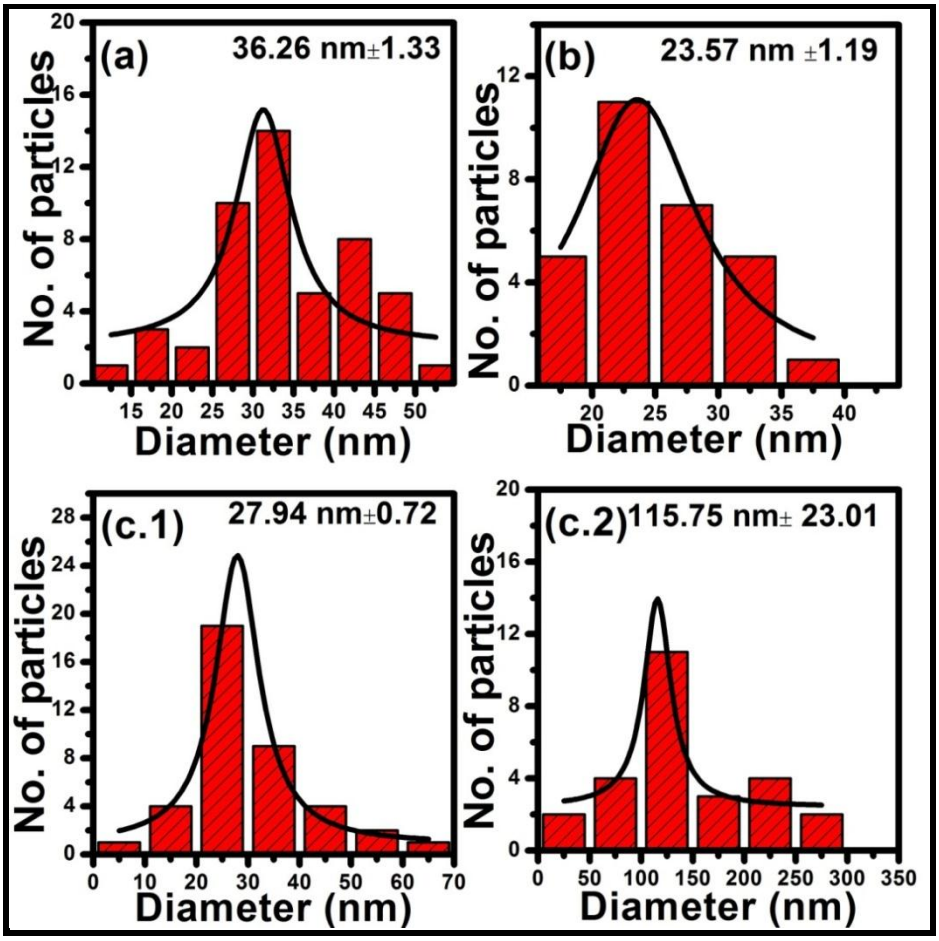

Figure 3.6: *particle size distribution histogram of (a) α-MnO_2, (b) β- MnO_2, (c.1) phase 1 and (c.2) phase 2 of αβ- MnO_2 nanorods.*

3.2.4 UV Visible Spectroscopy

We have examined the absorption behaviour of α-, β- and αβ-MnO_2 nanorods using UV visible spectroscopy in the wavelength range of 200-800 nm as shown in figure 3.7. The spectra show a broad absorption band in the region 300 to 600 nm with a peak at 370, 360 and 390 nm for α-, β- and αβ-MnO_2 nanorods, respectively which is attributed to the d-d transition of Mn ions [153]. In the ligands of MnO_6 octahedra, Mn 3d energy level split into the higher (e_g) and lower (t_{2g}) energy levels and the difference between them results in the optical band gap [134]. The band gap of α-, β- and αβ-MnO_2 nanorod is estimated using Tauc and Davis-Mott relation [154]:

$$(\alpha h\nu)^n = A(h\nu - E_g) \qquad [3.1]$$

where A is constant, hν is the phonon energy, E_g is the band gap and α is the absorption coefficient. n = ½ for indirect interband transition and n = 2 for direct allowed transition. We fit it taking n = ½ to calculate indirect band gap energy. The band gap energy calculated form the intercept of the linear position with energy axis at α = 0 is found to be 1.53, 1.30 and 1.45 eV for α-, β- and αβ-MnO_2 nanorods, respectively. Previously, *Li et al*. have observed a bandgap of 0.98 eV and 0.84 eV in α-MnO_2 nanowires of diameter 30 nm and 20 nm exposed with (110) and (210) planes, respectively [153]. *Gao et al.* have reported a band gap of 1.32 eV in α-MnO_2 nanofibers with diameter of 20-60 nm [155]. *Cockayane et al.* also theoretically calculate a bandgap of 1.29 eV for α-MnO_2 using density functional theory [156]. It is known that the increase in bandgap is associated with decrease in size of semiconducting material. In MnO_2, the valance of Mn is shown to affect the bandgap as well [156]. Although, the size of nanorods in β-MnO_2 is found to be smaller than α-MnO_2, the band gap observed in α-MnO_2 however defies the general observation.

Thus, high bandgap in α-MnO_2 clearly indicate that not only the size, but also the presence of Mn^{3+} in α-MnO_2 affects the band gap. The high Mn^{3+} concentration thus contributes towards higher bandgap in α-MnO_2 than β-MnO_2 although the size of nanorod is higher in the former one.

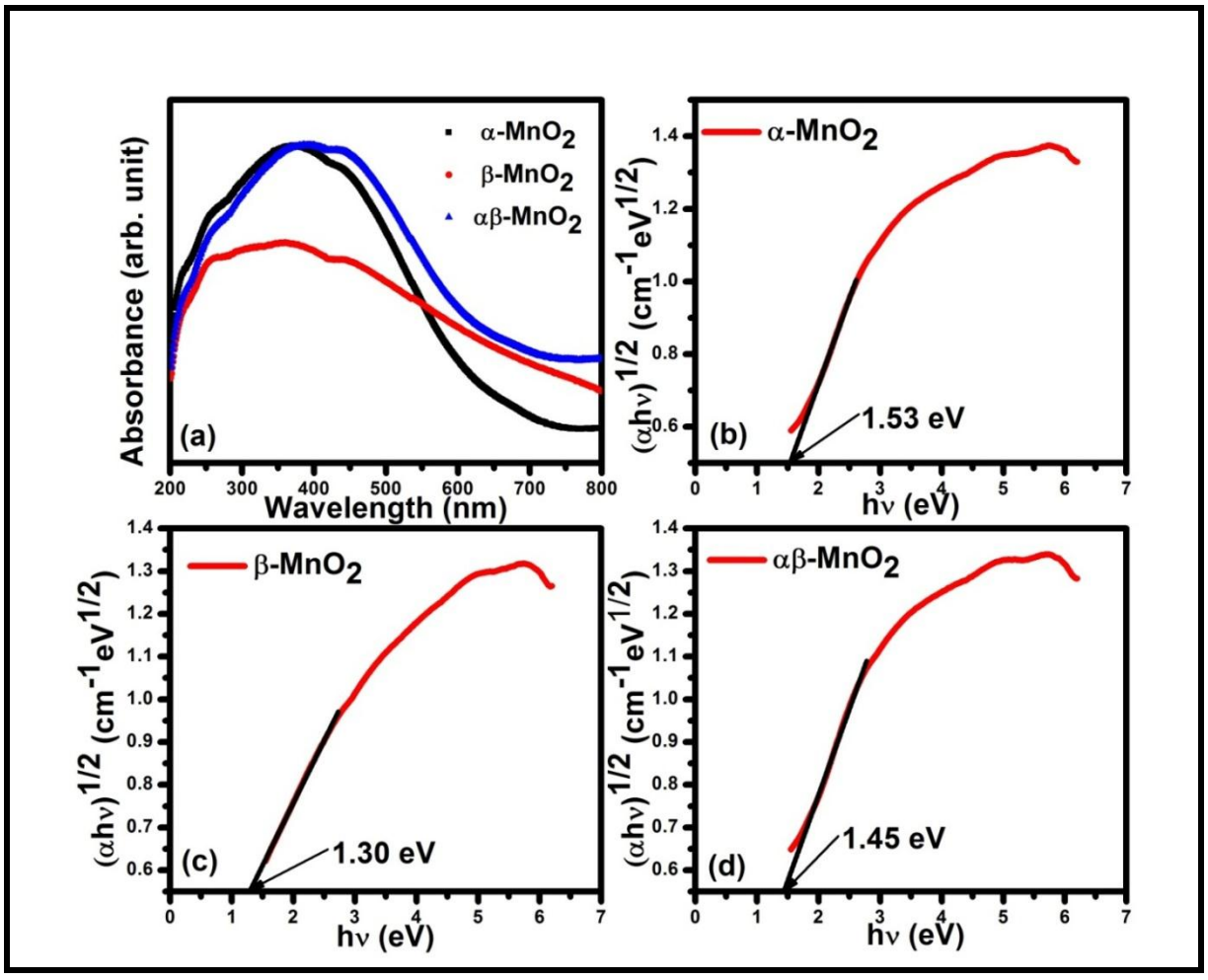

Figure 3.7: *(a) UV-visible absorption spectra of α-, β- and αβ-MnO_2 nanorods. Tauc plot and the corresponding linear fit for the calculation of optical bandgap of (b) α-MnO_2, (c) β-MnO_2 and (d) αβ-MnO_2 nanorods.*

3.2.5 X-ray Photoelectron Spectroscopy

Figure 3.8 depicts X-ray photoelectron spectra for Mn 2p and O 1s of α, β and αβ-MnO_2 nanorods. We have fitted the spectra with Gaussian-Laurentzian function using XPS software peak 4.1 with a straight background and have calibrated with carbon 1s peak at 284.8 eV. Figure 3.8(a-c) shows the Mn spectrum having two strong peaks attributed to Mn $2p_{3/2}$ and Mn $2p_{1/2}$ at ~ 642 eV and ~ 654 eV, respectively which agree well with those of the reported values [157]. The energy difference of 11.7 eV between Mn $2p_{3/2}$ and Mn $2p_{1/2}$ peak although confirms Mn^{4+}, the deconvolution of Mn $2p_{3/2}$ peak at ~ 542.5 eV and ~ 644.5 eV demonstrate the presence of +3 and +4 oxidation state of Mn in α, β, and αβ-MnO_2 nanorods, respectively. Irrespective of phase, Mn^{3+} is present along with Mn^{4+} ion. The area ratio of the peaks corresponding to +3 and +4 oxidation state of Mn gives the information of Mn^{3+}/ Mn^{4+} (Table 3.2) among α, β, and αβ-MnO_2 nanorods. While the concentration of Mn^{3+} is highest in α-MnO_2, an intermediate concentration in αβ-MnO_2 is obtained followed by β-MnO_2 nanorods. Further, the presence of Mn^{3+} is associated with oxygen vacancy which is determined from O 1s spectrum. The spectrum is deconvoluted into two peaks as shown in figure 3.9. The main characteristic peak (O_a) at ~ 529 eV and a soldier peak (O_b) at ~ 532 eV represent the presence of lattice oxygen and surface oxygen, respectively. The large area ratio of O_b and O_a in αβ-MnO_2 nanorods (Table 2) confirms the presence of oxygen vacancies at large scale.

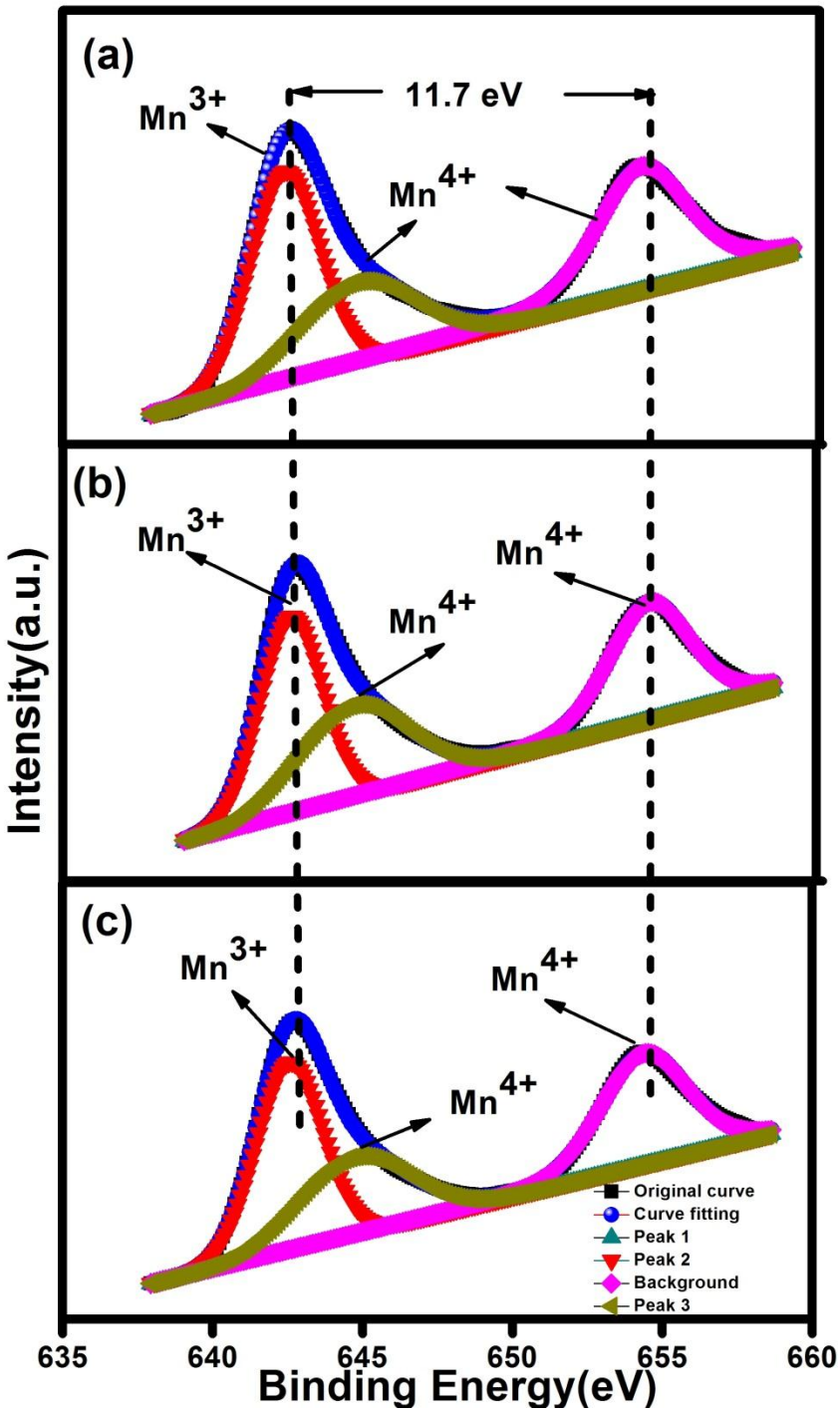

Figure 3.8: *X-Ray photoelectron spectra of Mn 2p for (a) α-MnO_2, (b) β- MnO_2 and (c) αβ-MnO_2 nanorods.*

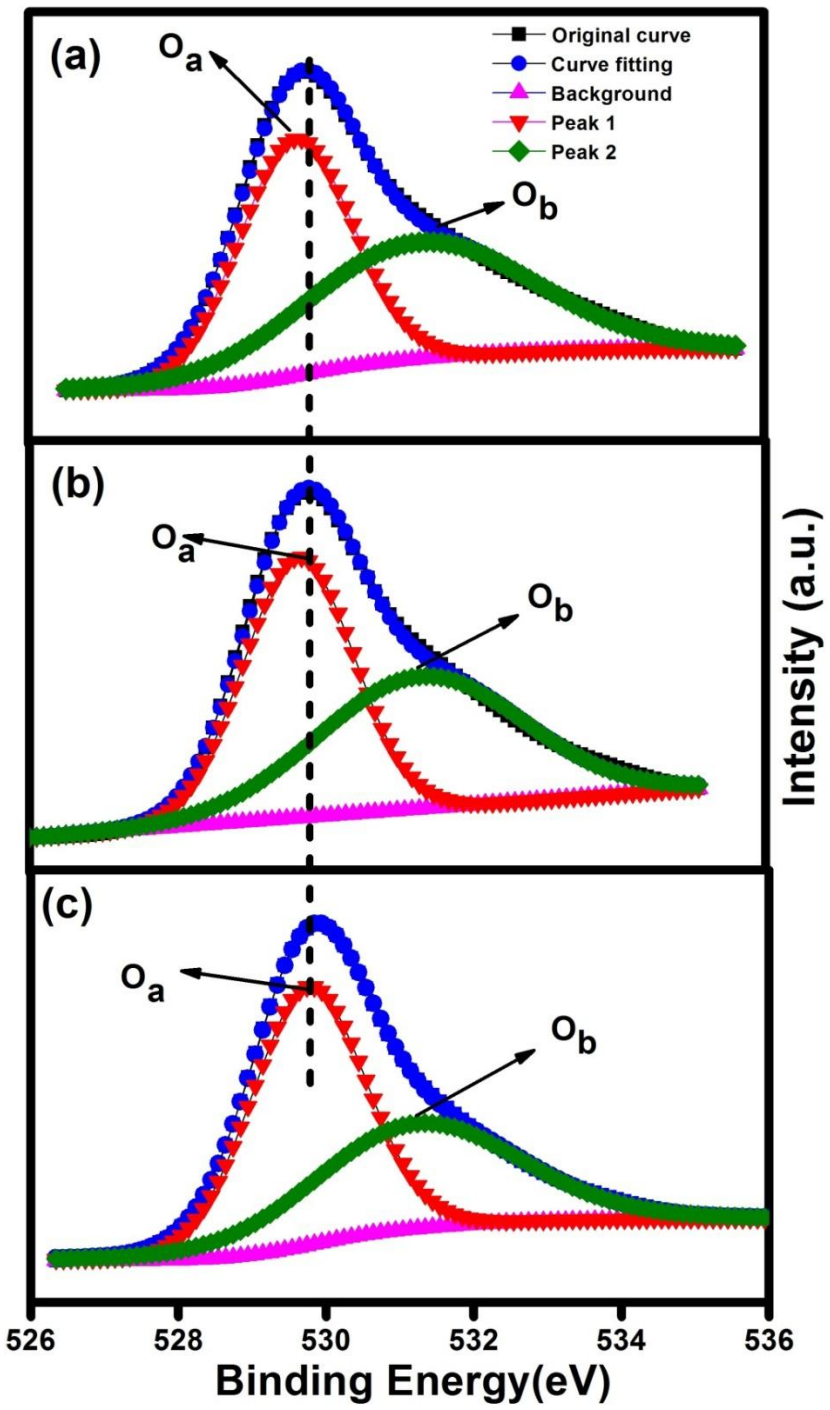

Figure 3.9: *X-Ray photoelectron spectra of O 1s for (a) α-MnO_2, (b) β- MnO_2 and (c) αβ-MnO_2 nanorods.*

Table 3.2: Mn^{+3}/Mn^{+4} and O_b/O_a obtained from fitting of Mn 2p and O 1s XPS peaks using software XPS peak 4.1 for α-MnO_2, β- MnO_2 and αβ- MnO_2 nanorods.

S.No.	Sample	Mn $2p_{3/2}$ (+3) B.E. ~642 eV	Mn $2p_{3/2}$ (+4) B.E. ~644 eV	Mn^{+3}/Mn^{+4}	O_a B.E~529 eV	O_b B.E~530 eV	O_b/O_a
		Peak area (%)			Peak area (%)		
1	α-MnO_2	61.74	38.25	1.61	49.98	50.01	1.00
2	β-MnO_2	55.65	44.35	1.25	51.49	48.51	0.94
3	αβ-MnO_2	59.74	40.25	1.48	56.82	43.17	1.31

3.3 Electrochemical Performance Using Cyclic Voltammetry

MnO_2 has been extensively investigated as a supercapacitor electrode material. Cyclic voltammetry (CV) measurement is employed to determine the electrochemical performance of α-MnO_2, β-MnO_2 and αβ-MnO_2 electrode material. Figure 3.10 depicts the nearly rectangular CV curve for α, β and αβ-MnO_2 nanorods at the scan rate of 20 mV/sec signifies the pseudocapacitive behaviour of the electrodes exhibiting fast reversible redox reactions [158]. Absence of any characteristics redox peak in CV curve indicates the pseudoconstant rate of charge discharge cycles. The specific capacitance from the CV curve is calculated using following equation [129]:

$$C = \frac{\int Idv}{(m \times \Delta v \times V)} \qquad [3.2]$$

Where, I is the voltammetric current (A), m is the mass of active electrode material (g) grafted on electrode surface, Δv is the potential window of CV curve and V is the potential scan rate (mV/sec). From above equation, one may note that, larger is the integrated area of the CV curve is the specific capacitance. Among, α, β and αβ-MnO_2 nanorods, β-MnO_2 nanorods show a largest integrated area of the CV curve followed by α-MnO_2 and αβ-MnO_2 nanorods. Large specific capacitance of β-MnO_2 nanorods is due to a rapid insertion/desertion of cations between electrode and electrolyte. Such fast transport could be due the small aspect ratio of nanorods where the surface is high. Therefore, the specific capacitance of β-MnO_2 is higher compared to α-MnO_2 and αβ-MnO_2. Although, α-MnO_2 show high specific capacitance than β-MnO_2 due to its large tunnel size (2X2) in bulk, due

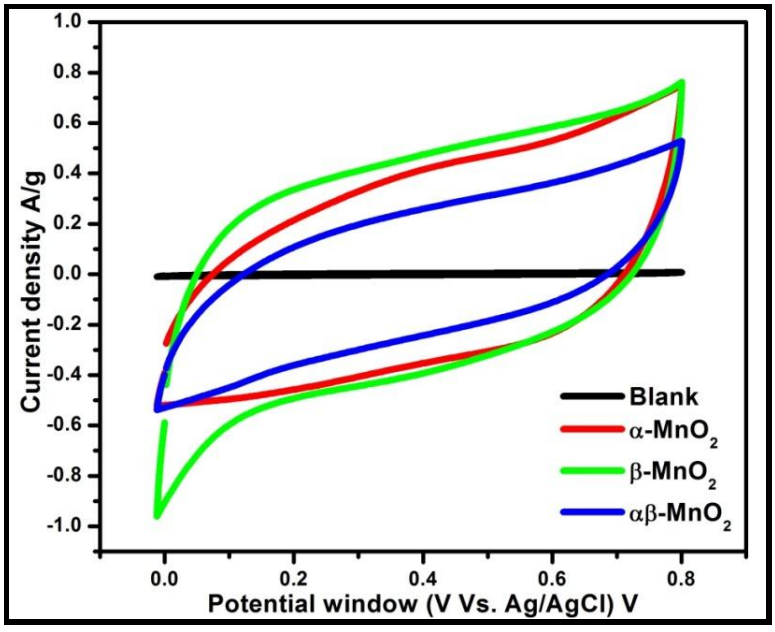

Figure 3.10: *Cyclic voltammogram of as prepared α-MnO_2, β- MnO_2 and αβ- MnO_2 nanorods at the scan rate of 20 mV/sec.*

to small size of nanorods in β-MnO_2, we observe a high capacitance in comparison to α and αβ-MnO_2 nanorods in the present case [107][159]. Further, the magnetic properties of these compounds are analysed.

3.4 Magnetic Properties

To study the magnetic properties of α-MnO_2, β-MnO_2 and αβ-MnO_2 synthesised at different potassium concentration, the temperature dependent and magnetic field dependent magnetization, temperature dependent ac susceptibility and remanant magnetization are carried out and discussed in section 3.4.1, 4.4.2, 3.4.3 and 3.4.4, respectively.

3.4.1 Temperature Dependent Magnetization

Temperature dependent dc magnetization (M-T) under zero-field cooling (ZFC) and field cooling (FC) mode have been carried out with an applying field of 100 Oe and in between 2 to 300 K. The results are shown in figure 3.11. It is interesting to note that for α-MnO_2 nanorods, with reducing temperature from 300 K, both M_{ZFC} and M_{FC} curves are virtually identical showing paramagnetic behaviour upto an irreversible temperature, T_{irr} of approximately 46 K followed by maxima at 30 K, known as Neel temperature (T_N) (Figure 3.11(a)). In case of β and αβ-MnO_2 nanorods, both M_{ZFC} and M_{FC} curves bifurcate at 78 K and 48 K which on further decreasing temperature shows T_N at 70 K and 20 K, respectively (Figure 3.11(b & c)). The inverse of susceptibility (1/χ) taken from ZFC magnetization vs. temperature for α, β and αβ-MnO_2 nanorods are fitted with Curie-Weiss law i.e. $1/\chi$ = (T-θ_{cw})/C as shown in figure 3.12. It is observed that while Curie-Weiss temperature (θ_{cw}) is found to be -455 and -547 K in case of α, and αβ-MnO_2 nanorods, in β-MnO_2, θ_{cw} is 70 K. The large negative value of θ_{cw} in α and αβ-MnO_2 nanorods indicates a strong

antiferromagnetic interaction. However, the positive θ_{cw} in β-MnO_2 could be due to the weak antiferromagnetic exchange interaction between inter magnetic sublattices compared to the ferromagnetic interactions in the intra sublattice. Similar feature have been reported in $SmFe_{0.57}Ge_{1.33}$ and other layered structures [160]. Curie constants (C) are found to be 3.28, 1.57, 3.72 emu.K/mol.Oe, for α, β and αβ-MnO_2 nanorods, respectively. Further, we estimate the effective paramagnetic moment, μ_{eff}, from Curie Constant using the following equation

$$\mu_{eff} = \sqrt{3C}\mathrm{K_B} \,/\, (N_A\mu_B^2) \qquad [3.3]$$

where K_B is Boltzmann's constant and N_A is Avogadro's number [160]. μ_{eff} is found to be 5.12μ_B, 3.96μ_B and 5.64 μ_B for α, β and αβ-MnO_2 nanorods, respectively. While μ_{eff} for β-MnO_2 nanorods is nearly equal to that of the theoretical one, μ_{eff} in α and αβ-MnO_2 nanorods is found to be higher than that of the μ_{eff} of Mn^{4+} ion (3.87μ_B**)** [161]. Such high magnetic moment could be inscribe to the Mn^{3+} ions which has large magnetic moment (4.90μ_B) in a high spin state. The fraction of Mn^{3+} ions have been calculated using the following equation [162]

$$\mu_{eff}^2 = (1-y)\,[\mu_{eff}(Mn^{4+})]^2 + y\,[\mu_{eff}(\mathrm{Mn^{3+}})]^2 \qquad [3.4]$$

where y is the concentration of Mn^{3+} ions present in the sample. Based on electrostatic charge neutrality, the presence of Mn^{3+} ions signifies that oxygen vacancies are present in the material. Two Mn^{3+} ions will create an oxygen vacancy which reduces to $MnO_{2-\delta}$, where δ represents the oxygen vacancies. The concentration of Mn^{3+} found to be 1.24, 0.13 and 1.51 in α, β, and αβ-MnO_2 nanorods, respectively. Hence, the actual composition of α, β, and αβ-MnO_2 are reduced to α-$MnO_{1.48}$, β-$MnO_{1.86}$ and αβ-$MnO_{1.15}$, respectively.

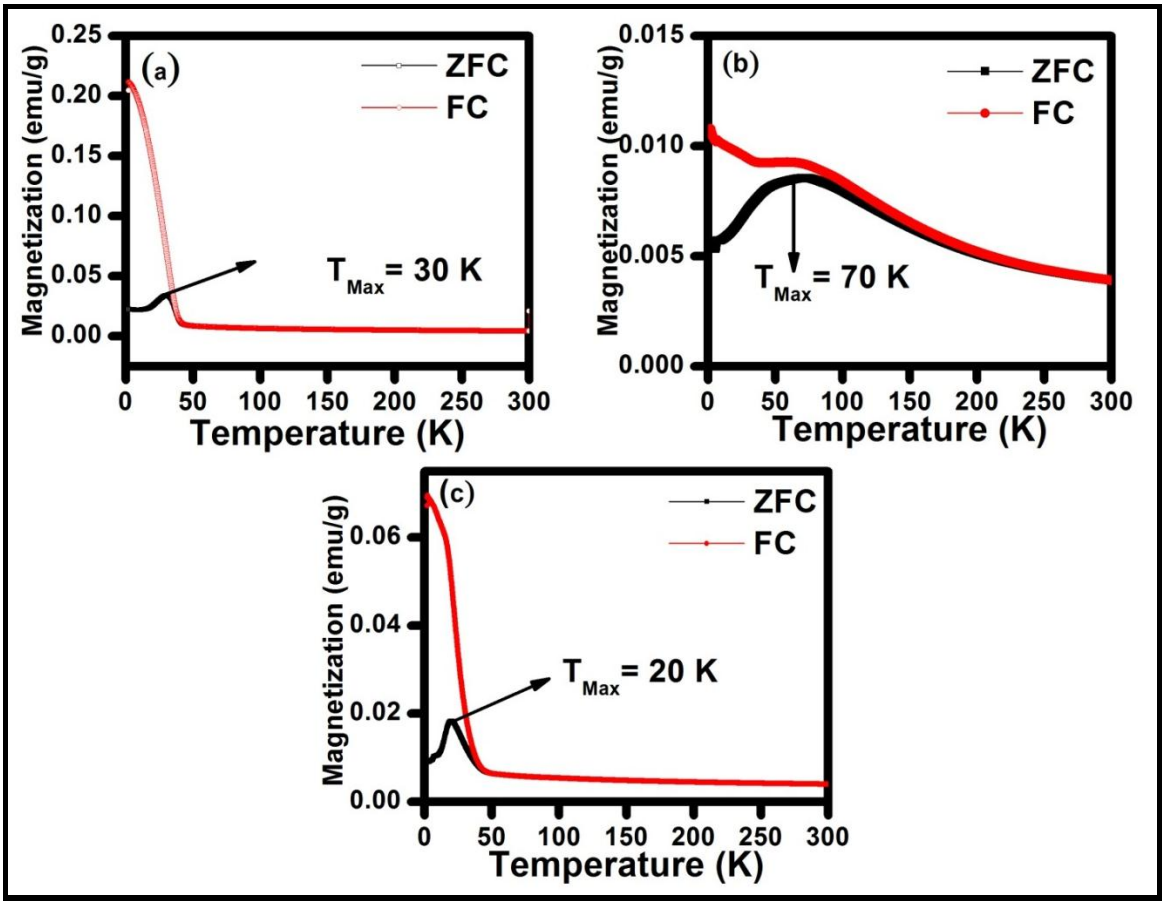

Figure 3.11: *Temperature dependent magnetization (M-T) curve of (a) α-MnO_2, (b) β-MnO_2 and (c) αβ- MnO_2 nanorods.*

3.4.2 Field Dependent Magnetization

Figure 3.13 depicts the magnetization (M) *versus* external magnetic field (H) for α-MnO_2, β-MnO_2 and αβ-MnO_2 nanorods at room temperature under ZFC condition in the range of ± 70 kOe. Absence of hysteresis in the magnetization curves shows the paramagnetic nature of the samples (not shown here). At 2 K, the magnetization curve shows a

hysteresis loop without any saturation even at high magnetic field (± 70 kOe) results from the large contribution of disordered spin at the surface.

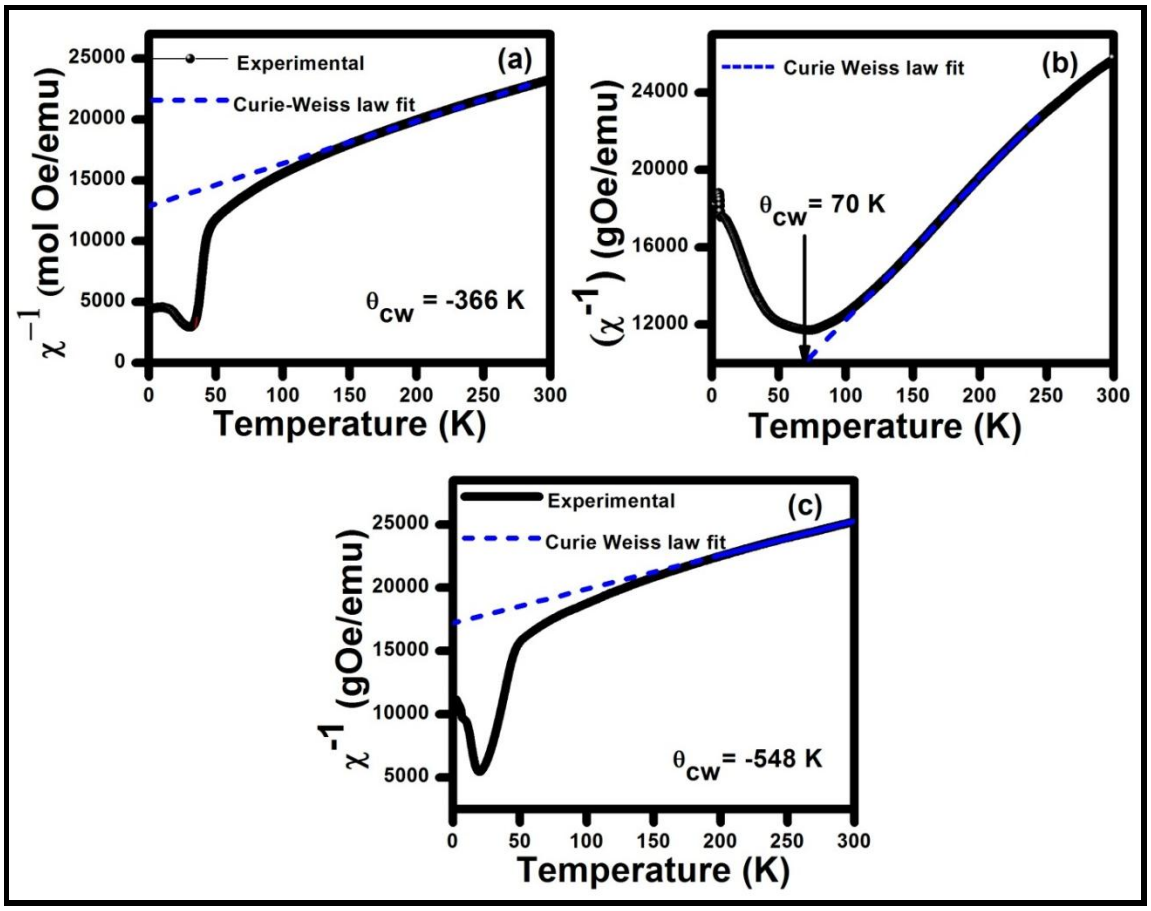

Figure 3.12: *Inverse susceptibility versus temperature fitted with Curie-Weiss law for (a) α-MnO_2, (b) β- MnO_2 and (c) αβ- MnO_2 nanorods.*

The effective coercive field is determined using $H_c^{eff} = \frac{(H_{c+} - H_{c-})}{2}$, where H_{c+} and H_{c-} are positive and negative magnetic field. We observe a coercive field of 4, 0.6 and, 2.7 kOe for α-MnO_2, β-MnO_2 and αβ-MnO_2 nanorods, respectively as shown in the inset of

figure 3.13. α-MnO_2 nanorods show high coercivity with large magnetization suggest the presence of a large number of canted AFM spins below T_N [163]. The remanant magnetization is found to be 0.008, 0.007 and 0.004 μ_B for α-MnO_2, β-MnO_2 and αβ-MnO_2 nanorods, respectively indicating no significant change in M_R with phase.

3.4.3 ac Susceptibility

To investigate the spin dynamics of the system, we have carried out frequency dependent ac susceptibility measurement to get better perspective of magnetically ordered state in α-MnO_2, β-MnO_2 and αβ-MnO_2 nanorods. The variation of real $\chi'(T)$ and imaginary $\chi''(T)$ with the temperature at 31, 101, 299 and 501 Hz are shown in figure 3.14.

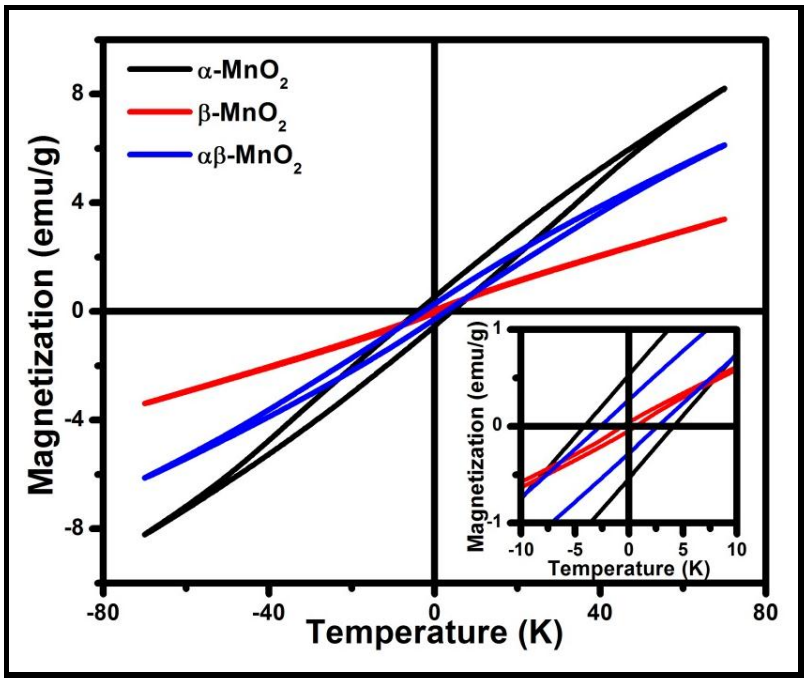

Figure 3.13: *Magnetization versus magnetic field at 2K for (a) α-MnO_2, (b) β- MnO_2 and (c) αβ- MnO_2 nanorods. Inset shows the enlarged view.*

In case of α-MnO_2 nanorods, no shift in the peak position of $\chi'(T)$ and $\chi''(T)$ have been observed (Figure 3.14a). Such behaviour eliminates the existence of spin-glass and superparamagnetic behaviour in α-MnO_2 nanorods. In case of β-MnO_2 nanorods, χ' displays a sharp peak at ~ 74 K and another diffused peak at 22 K. The former peak is frequency independent corresponding to a long-range ordering associated with antiferromagnetic transition [163], and the later one shows a frequency dispersion behaviour (figure 3.14b). Inset shows the shifting of peak towards higher temperature with frequency. It is interesting to mention that such magnetic anomaly could not be detected in dc magnetization measurement. Further, we have performed remnant magnetization measurement, to confirm spin-glass behaviour discussed later. In αβ-MnO_2 nanorods, peak in χ' and χ'' observed at ~19 K shifts towards higher temperature with frequency (figure 3.14c). Here, we conclude that except α-MnO_2, β and αβ-MnO_2 demonstrate frequency dispersion pertaining to spin-glass, cluster-glass and/or superparamagnetic behaviour. In our case, relatively small shift is observed in freezing temperature, T_f with frequency. It is known that T_f is less frequency dependent for SG and interacting SPM particles, whereas in case of non-interacting SPM particles, T_f is largely frequency dependent. The frequency dependence of T_f is analyzed employing the following relation:

$$\phi = \Delta T_f / T_f \Delta(\log\omega) \qquad [3.5]$$

where ϕ is the frequency sensitive parameter, Δ is the difference in related parameters, T_f is the spin freezing temperature at frequency, ω . It is generally accepted that ϕ lies in the range 0.005-0.08 for spin-glass (SG) [164], ~ 0.03-0.06 for cluster glass (CG) [165] and (0.1-0.13) for superparamagnetic (SPM) blocking [41]. The calculated ϕ value is found to

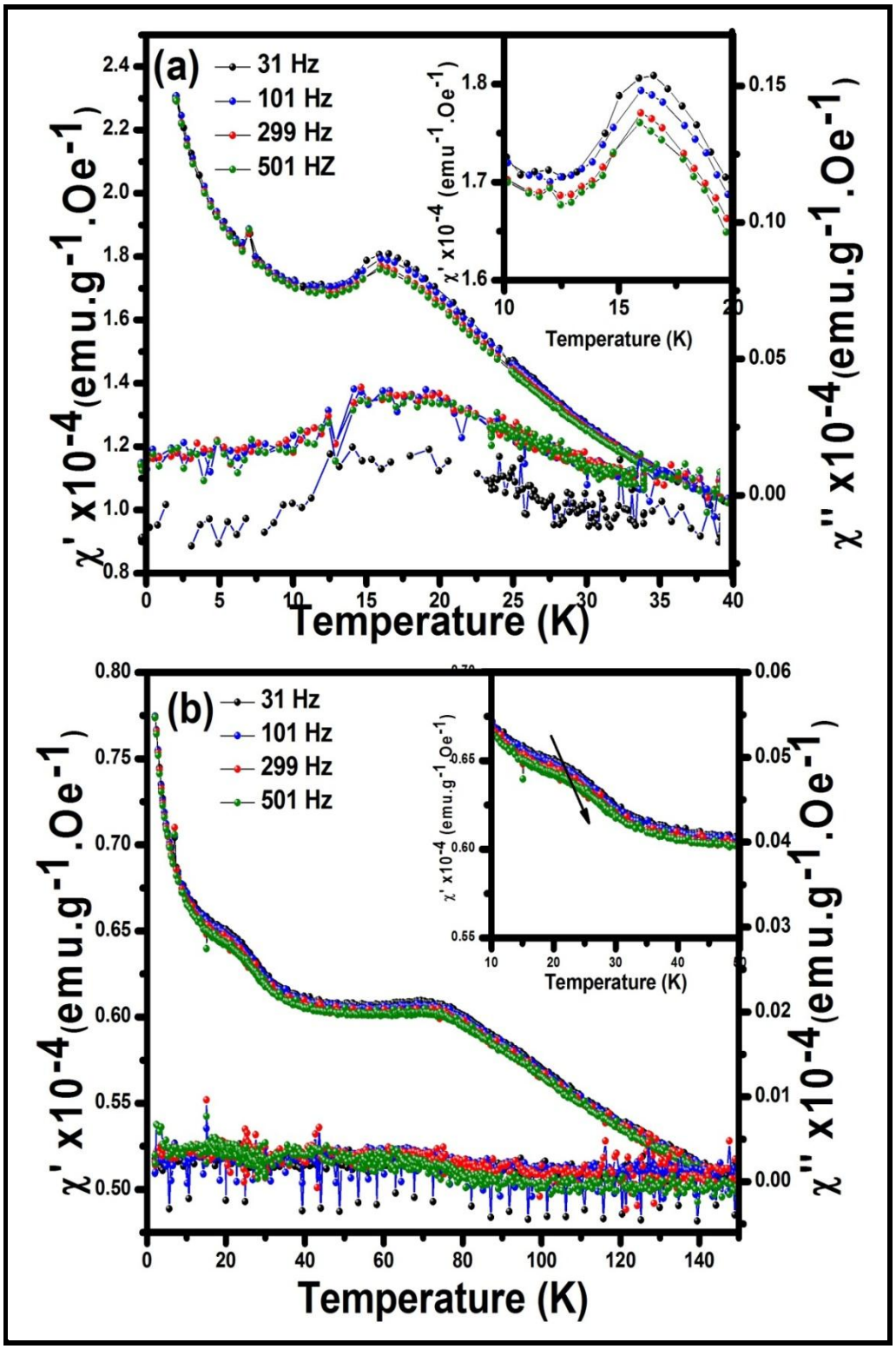
(a)
31 Hz
101 Hz
299 Hz
501 HZ
χ' x10-4(emu.g-1.Oe-1)
χ'' x10-4(emu.g-1.Oe-1)
Temperature (K)
χ' x10-4 (emu-1.Oe-1)
Temperature (K)
(b)
31 Hz
101 Hz
299 Hz
501 Hz
χ' x10-4(emu.g-1.Oe-1)
χ'' x10-4(emu.g-1.Oe-1)
Temperature (K)
χ' x10-4 (emu.g-1.Oe-1)
Temperature (K)

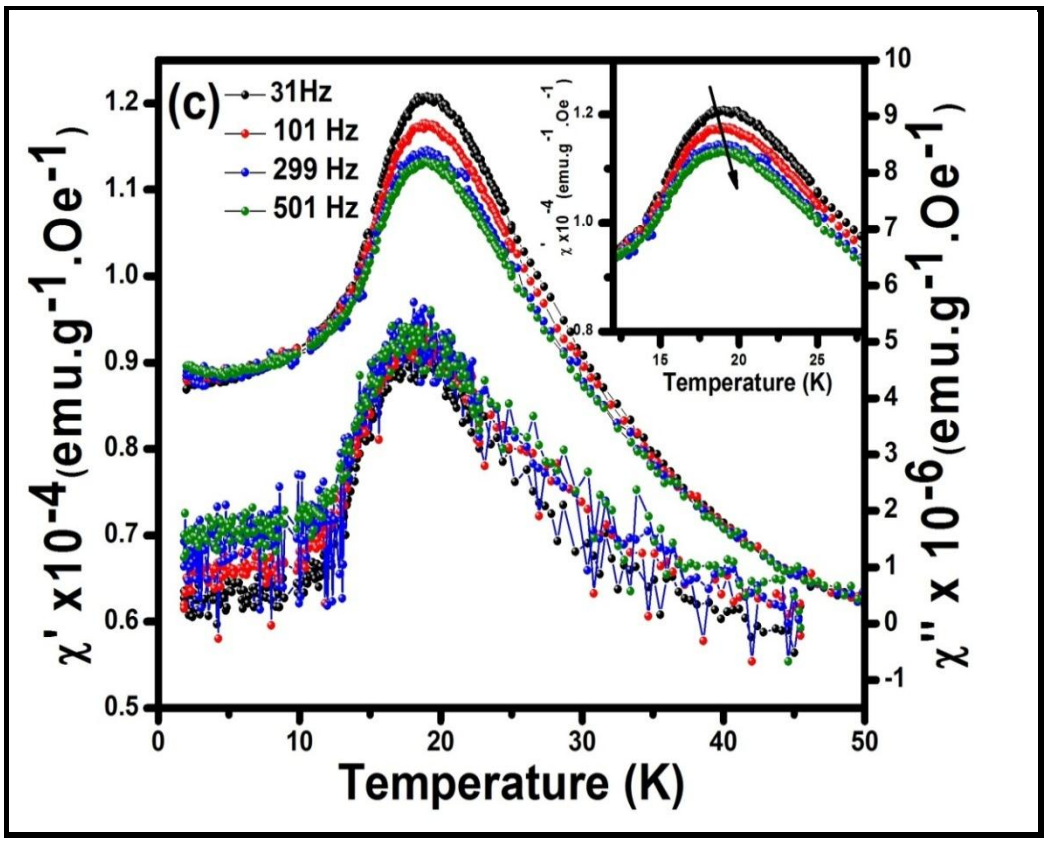

Figure 3.14: *Temperature dependence of real (χ') and imaginary (χ'') of ac susceptibility data at 31, 101, 299 and 501 Hz with an ac field of 3 Oe for (a) α-MnO_2, (b) β- MnO_2 and (c) αβ- MnO_2 nanorods and corresponding inset shows the enlarge view at peak position.*

be 0.0063 which is in good agreement with SG freezing instead of SPM blocking. To further understand intercluster interactions for getting additional insights into SG state, various phenomenological models like the Neel–Arrhenius, Vogel–Fulcher, and power law are verified. The relaxation time (τ) dependence of freezing temperature (T_f) is fitted by Neel-Arrhenius law as given below

$$\tau = \tau_o \exp\left(\frac{E_a}{K_B T}\right) \qquad [3.6]$$

where E_a is the activation energy barrier for spin flipping and K_B is the Boltzmann's constant [166]. The prefactor τ_o is the inverse of attempted frequency and usually found between ~10^{-10} and 10^{-13} s. The lnτ versus 1/T plot derived from the ac susceptibility data points are shown in figure 3.15(a). The best fit of our data gives unphysical value i.e. $\tau_o \sim 3.259 \times 10^{-68} \ll 10^{-13}$ s which further rules out the possibility of superparamagnetic blocking. We employ conventional critical slowdown of spin dynamics to understand the SG nature of the system at critical temperature as described by Power law. Therefore, we fit the data with Vogel-Fulcher law and Power law used for SG or CG systems shown in figure 3.15(b & c). Power law is used to determine the spin-glass freezing temperature, T_{SG} in the limit frequency, f→0. Therefore, we have analyzed this data using following Vogel-Fulcher law [167] and Power law [167] given below as equation 3.7 and 3.8, respectively.

$$\tau = \tau_{\circ} \exp\left(\frac{-E_{\circ}}{K_B(T_f - T_{\circ})}\right) \qquad [3.7]$$

$$\tau = \tau_o \left(\frac{T_f}{T_{SG}} - 1\right)^{-z\upsilon} \qquad [3.8]$$

where T_{SG} is the critical temperature for SG ordering lies between 0 and T_f . $\tau_{\circ}$ is the characteristic spin flipping time; zν is the dynamic critical scaling exponent related to correlation length ξ. The value of zν holds well in the range between 2 and 10 for spin-glass systems [167]. The parameters obtained from equation 3.7 and 3.8 are illustrated in Table 3.3. From Vogel- Fulcher law, the obtained high value of $\tau_{\circ}$ (10^{-9}s) is expected from interacting magnetic spin clusters as for SG, $\tau_{\circ}$ is typically lies between 10^{-11} and 10^{-13} s

and between 10^{-6} and 10^{-10} s for cluster-glass [168][169]. The T_{SG} and $\tau_{\circ}$ obtained from Power law and Vogel-Fulcher law indicates that the particles behaves like SG and/or CG.

Table 3.3: Fitting parameters deduced from ac susceptibility data fitted with Neel-Arrhenius law, Power law and Vogel-Fulcher law for αβ- MnO_2 nanorods.

Sample	**Neel-Arrhenius**		**Power Law**			**Vogel-Fulcher Law**		
	E_a/K_B (eV)	**$\tau_{\circ}$ (s)**	**T_{SG} (K)**	**zν**	**$\tau_{\circ}$ (s)**	**$T_{\circ}$ (K)**	**E_a/K_B (eV)**	**$\tau_{\circ}$ (s)**
αβ - MnO_2	2847.05	3.25×10^{-68}	17.30 ± 2.26	11.09 ± 2.54	2.94×10^{-13}	17.03 ± 0.2	23.57	2.89×10^{-8}

3.4.4 Remanent Magnetization Measurement

To further confirm such behaviour, we perform remanent magnetization measurement in FC mode. We cool the sample from 300 K to 5 K in a field of 100 Oe. After cooling the sample field was removed and magnetization decay (M_{RM}) was recorded as a function of time for a waiting period, t_w, as shown in figure 3.16. Remnant magnetization gives a nonzero magnetization that decays very slowly i.e. less than 3%, even after 13000 s. The decay behaviour reveals two regimes with different time responses, a rapid initial magnetization relaxation followed by a slower relaxation. We have fitted with stretched exponential decay equation as given below

$$M(t) = M_o + M_r \exp\left[-(t/\tau)^n\right] \qquad [3.9]$$

where M_o is the intrinsic static magnetization component, M_r is related to glassy component of observed relaxation effect, τ is the characteristic relaxation time and n is the stretched exponential [170]. If n = 0 then system has no relaxation, while if n = 1 then system has mono-dispersive Debye-like relaxation. The value of 'n' between 0 and 1 supports a different class of SG systems. From figure 3.16, it is clear that remanant magnetization of both β and αβ-MnO_2 nanorods follow the remanant magnetization decay.

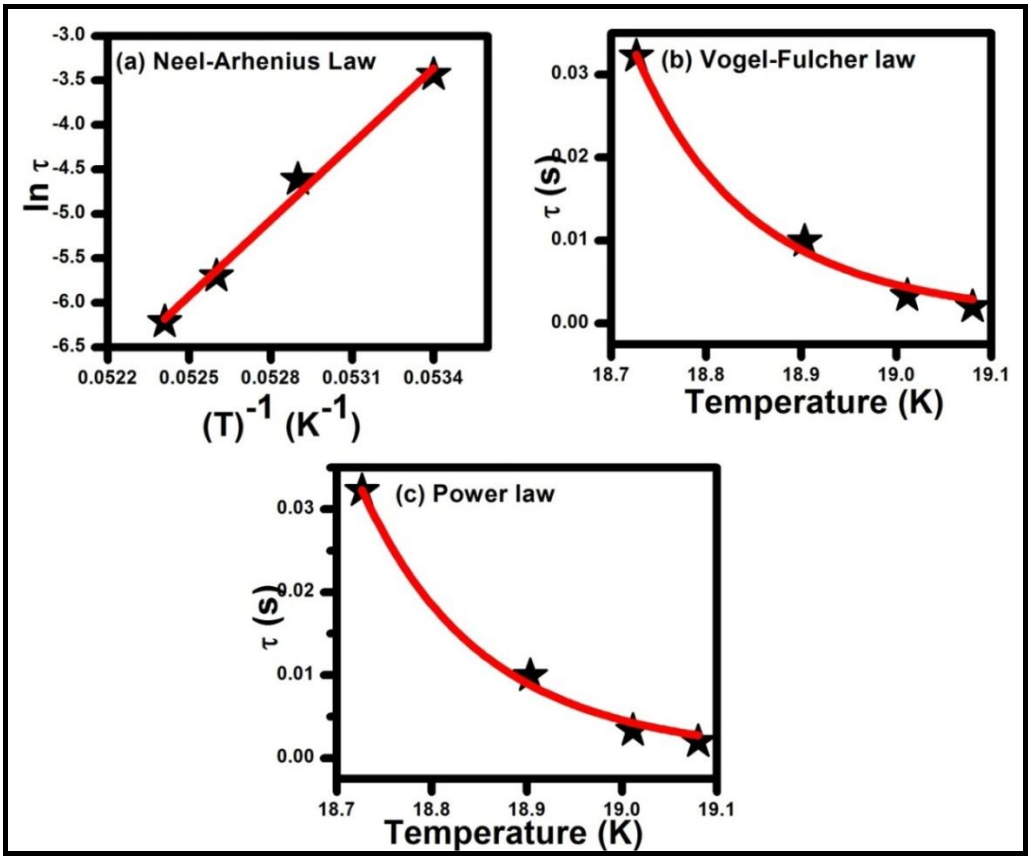

Figure 3.15: *Variation of relaxation time (τ) with temperature (T) plotted and fitted with (a) Neel-Arrhenius law (b) Vogel–Fulcher law and (c) Power law for αβ- MnO_2 nanorods. Solid line represents the fitting.*

The fitting parameters, M_o, M_r, t and n for β-MnO_2 and αβ-MnO_2 nanorods are illustrated in Table 3.4. Observed relaxation time (t) and exponent (n) are in good agreement with the values reported for SG like systems. Spin-glass behaviour in $Ba_{1+\delta}Mn_8O_{16}$ and α-MnO_2 is attributed to the geometrical frustration in a triangular lattice and complex interactionbetween mixed-valence of Mn^{4+} and Mn^{3+} as reported by *Yu et al.* [103] and *Luo et al.* [3], respectively. SG behaviour in δ-MnO_2 nanowhiskers is contributed by the interaction between Mn^{4+} and Mn^{3+} [171]. Thus, the spin freezing obtained in the present case is attributed to the interaction of Mn^{3+} and Mn^{4+} ions. However, it is interesting to note that we have not observed SG behaviour in α-$MnO_{1.48}$ though Mn^{3+} is present. The oxygen vacancies are more than β-MnO_2 and less than αβ-MnO_2 nanorods. It is thus clear that within a certain concentration of Mn^{3+}, its contribution towards SG/cluster-glass behaviour is insignificant.

Table 3.4: Fitting parameters deduced from thermoremanent relaxation magnetization fitted with stretched exponential decay function for (1) β- MnO_2 and (2) αβ- MnO_2 nanorods.

S.No.	Sample	Stretched exponential function			
		M_o (emu/g)	M_r (emu/g)	T (s)	n
1.	β-MnO_2	0.0037	0.0082	2755.55	0.3679
2.	αβ-MnO_2	0.023	0.0012	4046.62	0.4382

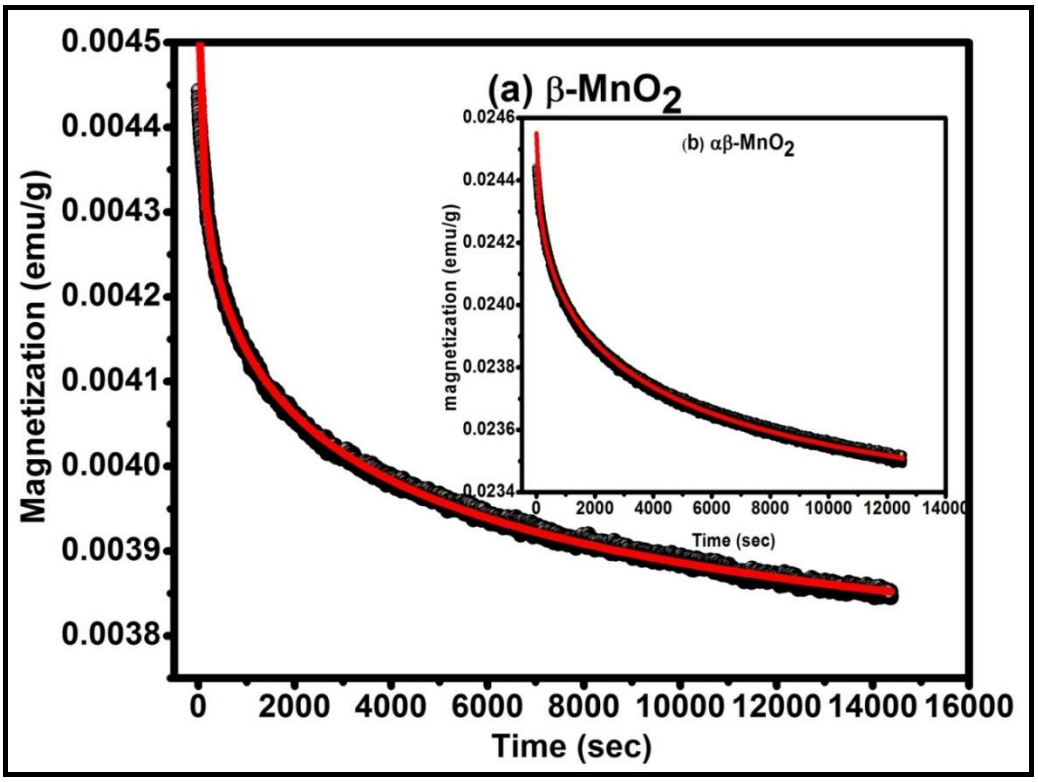

Figure 3.16: *Thermoremanent magnetization measurement at 5 K fitted with stretched exponential decay functions for (a) β-MnO_2 and (b) αβ-MnO_2 nanorods.*

3.5 Conclusion

Polymorphs of MnO_2 such as α, β and mixed phase of α and β phase of MnO_2 were synthesised via hydrothermal technique by varying the concentration of $KMnO_4$. The structure, electrochemical performance, optical and magnetic properties of these nanomaterials were explored. XRD and FTIR spectroscopy confirmed the pure phase formation of MnO_2. Through Rietveld refinement, we determined the phase fraction of α and β phase which were found to be ~73% and ~27%, respectively in αβ-MnO_2. Field

emission scanning electron micrographs showed the formation of nanorods irrespective of the phase. While α, and β-MnO_2 nanorods were grown with an average diameter of 28 and 116 nm in αβ-MnO_2, two different aspect ratio of nanorods were attributed to the presence of α and β-MnO_2 phase. Small size of nanorods in β-MnO_2 resulted high specific capacitance in comparison to α- and αβ-MnO_2 nanorods. The optical bang gap estimated through UV-visible spectra for α-, a β- and αβ-MnO_2 nanorod was found to be 1.53, 1.30 and 1.45 eV, respectively. We studied the dynamic magnetic properties of α-MnO_2, β-MnO_2 and αβ-MnO_2 nanorods by performing DC magnetization, frequency dependent ac susceptibility and relaxation remanant magnetization. The negative Curie-Weiss temperature (θ_{cw}) while confirmed the antiferromagnetic ordering in α-MnO_2 and αβ-MnO_2, positive θ_{cw} in β-MnO_2 showed strong ferromagnetic interaction due to dominating intra sublattice interaction. No shifting of the peak in $\chi'(T)$ ruled out the presence of spin-glass behaviour in α-MnO_2 nanorods. However, in β-MnO_2 and αβ-MnO_2 T_f observed at 22 K and 19 K absent in M Vs. T curve showed frequency dispersion behaviour. Fitting susceptibility with Vogel-Fulcher, Power law and remanant magnetization measurement, we concluded that spin-glass and/or cluster-glass feature as observed in β- and αβ-MnO_2 nanorods. It was important to mention here that, such SG behaviour was critical towards the presence of Mn^{3+} in MnO_2 compound which also affects the bandgap of the material.